Analysis of the diffraction-line broadening on nanostructured Fe: size–strain effects induced by milling and heating

Analysis of the diffraction-line broadening on nanostructured Fe: size–strain effects induced by milling and heating

David Martínez-Blanco[1,2], Pedro Gorria[1], Jesús A Blanco[1], María José Pérez[1] and Javier Campo[3,4]

[1] Departamento de Física, Universidad de Oviedo, Calvo Sotelo, s/n, 33007 Oviedo, Spain

[2] Unidad de Medidas Magnéticas, SCT, Universidad de Oviedo, Julián Clavería, s/n, 33006 Oviedo, Spain

[3] Instituto de Ciencia de Materiales de Aragón, CSIC-Universidad de Zaragoza, 50009 Zaragoza, Spain

[4] Institut Laue-Langevin, BP 156, F-38042 Grenoble Cedex 9, France

E-mail: pgorria@uniovi.es

Abstract

The microstructure of ball milled Fe powder as a function of the milling time has been investigated using room temperature x-ray powder diffraction and transmission electron microscopy. The powder microstructure changes when the milling time increases in a twofold way: (i) a reduction of the crystalline grain size to around 20 nm after 80 h of milling time and (ii) a significant amount of microstrain is induced (up to ∼0.75%), together with a slight increase of the crystalline lattice parameter. Moreover, the temperature dependence of the microstructure has been studied by means of *in situ* neutron powder thermo-diffraction in the range between 300 and 1220 K for the sample milled for 80 h. The heating of the nanostructured powder produces a progressive grain growth starting at around 450 K, and the disappearance of the microstrain above 850 K due to relaxation processes induced by thermally activated atomic diffusion. The kinetics of both processes at two different heating rates of 1 and 10 K min^{-1} has been compared. A detailed analysis of the diffraction patterns has been performed using the Rietveld method. All this microstructural information can be correlated with the temperature dependence of the magnetization of nanostructured Fe and the differences found with regard to the case of bulk Fe.

(Some figures in this article are in colour only in the electronic version)

1. Introduction

In the last two decades, we have witnessed a rapid growth in research and development of nanoscience and nanotechnology, especially focused in the synthesis of new nanostructured materials exhibiting amazing physical response for technological applications [1, 2]. In this way, the evolution of new magnetic materials has been shifted to the nanocrystalline regime [3]. This is particularly true in the case of soft magnetic materials [3–6]. Among them, the comprehension of iron magnetism in a nanostructured state is a recent field of research with still some open questions, especially those related to the link between microstructure and magnetic behaviour [7–10]. On the other hand, the complete understanding of such a simple system is a previous fundamental step for the study of more complex Fe-based compounds inside this scenario [11–14]. One of the simplest methods to produce nanostructured materials is the ball milling (BM) technique [15], that allows us to obtain massive samples in powder form and of several grams in mass [16, 17]. The processing conditions involved during the preparation of such materials have a significant effect on the microstructure and physical properties [18–24]. Furthermore, BM produces a huge number of defects [25] and a large decrease of the average

grain size of the crystallites, even below 30 nm, together with mechanically induced disorder [26–28]. In particular, this reduction in the 'crystalline size' (coherent diffraction domains) and the occurrence of microstrains [29], which both broaden the Bragg peaks of the diffraction pattern, can be attributed to an increase of the density of dislocations. In the case of pure Fe subjected to high-energy ball milling, this procedure gives rise to changes in the magnetic response, depending on parameters such as milling speed, milling time, or the ball-to-powder mass ratio [30–35].

Nowadays, valuable microstructural information can be extracted from x-ray and/or neutron powder diffraction through the detailed analysis of the patterns. This analysis is usually performed via the Rietveld method (RM) [36] and/or the RM with Fourier transform to describe the broadening of the Bragg peaks. Using a certain peak shape and a mathematical expression for the variation of the FWHM with the Bragg diffraction angle, the size of structural domains and also their average shape with anisotropic models based on Popa rules [37–40] can be described. This procedure allows us to fit the whole pattern, and from its angular dependence the size and microstrain contributions can be separated. To achieve this purpose, it is necessary to start with a good quality first model, hence a two-stage approach is commonly followed [41]: first, parameters which describe intensity, position, width and shape of some individual peaks are obtained by pattern decomposition without any structural information; second, with these results we design an appropriate model with all the structural parameters joined, and then it is refined in a whole pattern calculation.

Once we have applied the two-stage procedure to analyse the XRD patterns of our ball milled nanostructured Fe powder samples by Rietveld refinement, using the Fullprof Suite package [42], the results are combined with the observed microstructure in transmission electron microscopy (TEM) images. Besides this, a neutron thermo-diffraction (NTD) study was performed in samples milled for a longer period of time (80 h) and at two distinct rates of heating (1 and 10 K min^{-1}). This kind of '*in situ*' experiment, not reported up to now in Fe milled samples, gives the possibility to study the microstructural changes occurring during thermal relaxation of the sample. This experimental procedure provides more accurate information on such process compared with that obtained, usually at room temperature, from samples milled and further annealed at fixed temperatures [43]. Finally, a discussion of the correlation between the observed magnetic behaviour and the change of the microstructural parameters with temperature is stressed.

2. Experimental techniques

Samples were prepared under Ar atmosphere using a high-energy planetary ball mill (Retsch PM400/2), introducing inside the stainless steel vessels Fe standard powders (99.9% purity) 60 μm in average macroscopic size with stainless steel balls 10 mm in diameter, in a ball-to-powder weight relation of 8:1. The angular velocity was 200 rpm. The milling procedure was carried out following successive steps of 10 min

of clockwise and anti-clockwise rotation with 5 min break in between in order to avoid possible re-crystallization processes due to temperature rising. Some portion of the samples was removed from the vessels after selected milling times and prepared for the XRD measurements. The samples will be named hereafter Fe-*x*h, where $x = 4, 10, 16, 30, 45, 60, 75$ and 80 h and denotes the effective time of milling. It is worth noting that using balls and vessels both made of WC under the same conditions the milled powders show the same structural characteristics, thus discarding possible Fe, Cr or C contamination effects as reported by other authors [44–46].

The x-ray diffraction patterns were collected on a Seifert XRD 3000 diffractometer in Bragg–Brentano geometry at room temperature (RT). We have employed two x-ray wavelengths, the double Kα radiation $\lambda = 1.5418$ (0.7107 Å) of a Cu (Mo) anode, incident and receiving slits of 1 mm and 0.1 mm, respectively, and a secondary pyrolytic graphite monochromator was placed before the scintillation detector for removing the fluorescence radiation. Vertical Soller slits were also used after the primary and secondary slits to delimit the vertical divergence. The angular range spread over the region between 20° and 160° in 2 theta (2θ), with a step of 0.02°. Time counting of 30 s per step was used in order to obtain good statistics. NTD experiments in the Fe-80h sample were performed on the high-flux D1B two-axis neutron powder diffractometer (Institut Laue–Langevin, Grenoble, France), using a neutron wavelength of $\lambda = 1.28$ Å selected from a germanium (311) monochromator. This instrument permits us to perform real-time thermo-diffraction experiments over a wide temperature range in a few hours [47, 48]. These characteristics make D1B a useful tool for the '*in situ*' study of structural transformations. Two portions (5 g each) of the as-milled sample were introduced into cylindrical sample holders and then located inside the furnace, both vanadium made. During continuous heating ramps at two different rates of heating, 1 and 10 K min^{-1}, between 300 and 1220 K, we collected a diffraction pattern each 5 min (1 min) for the 1 K min^{-1} (10 K min^{-1}) rate. The available angular range, 2θ, for the ^{3}He multidetector containing 400 cells is 80° (steps of 0.2°), and we selected the measuring interval between 25° and 105°. All the x-ray and neutron powder diffraction patterns can be indexed within the body-centred cubic (bcc) crystal structure (space group $Im\bar{3}m$, No 229).

Both particle size and shape of the Fe-80h sample were obtained by TEM (180 keV JEOL-2000 EX-II). For the TEM analysis, the powders were dispersed in ethanol and a drop of this suspension was deposited onto a carbon-coated copper grid. After counting a large number of particles from several TEM images, the histogram corresponding to the particle-size distribution was obtained. The fit to a log-normal distribution gives the particle mean size and the standard deviation. Magnetization curves, $M(H)$, up to 70 kOe were measured at RT using a Quantum Design SQUID magnetometer at the University of Zaragoza. Finally, magnetization versus temperature curves, $M(T)$, were obtained in the temperature range from 290 to 1100 K and at an applied magnetic field of $H = 1$ kOe by means of a Faraday balance at the University of Oviedo.
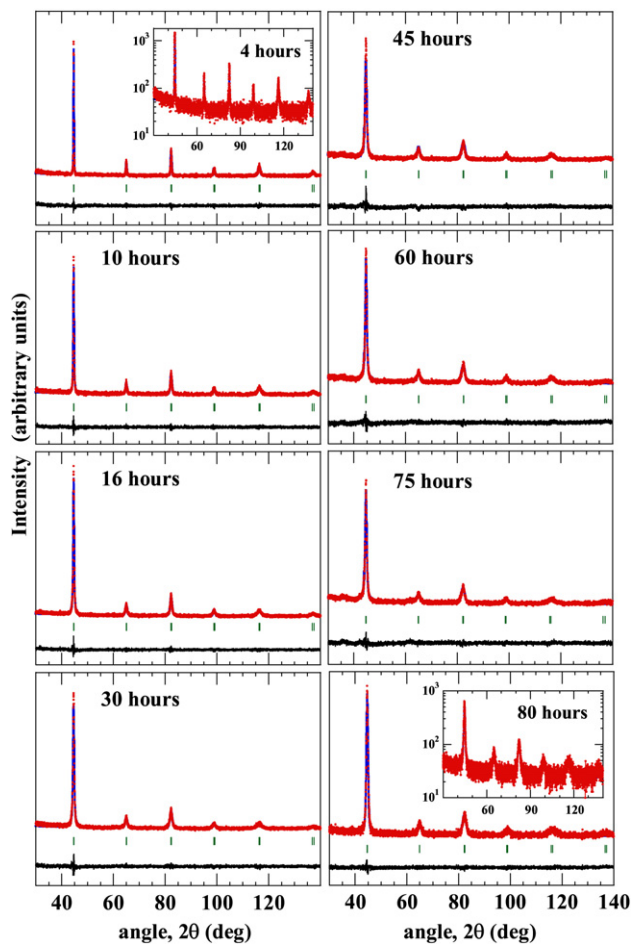
Figure 1. Observed (points) and calculated (solid line) room temperature x-ray powder diffraction patterns of Fe for different milling times ($\lambda = 1.5418$ Å). Positions of the Bragg reflections are represented by vertical bars. The observed–calculated difference pattern is depicted at the bottom of each figure. The insets show the patterns corresponding to Fe-4h and 80h samples using a log-scale for the intensity.

3. Results and discussion

The details of the procedure used for the analysis of the size–strain line broadening obtained from the diffraction patterns are summarized in the appendix. For the study of Fe as-milled samples the best choice for the profile instrumental resolution function (IRF) is that obtained from the Fe standard powders, on the basis of these two reasons: first, the IRFs determined using both XRD and NTD data on the Fe standard material lead to one of the best refinements compared to those obtained for the other investigated standard samples (Si, KCl, Cu, ...; see the the appendix); second, in this kind of microstructural analysis the use of a standard sample with similar structure to that of the samples under study is needed in order to define as well as possible the IRF near to the Bragg reflections, a condition that is fulfilled by the Fe standard sample.

3.1. Evolution of the microstructure with the milling time: XRD pattern analysis

Once the IRF had been determined for both diffractometers, we started with the two-stage approach of the XRD pattern,
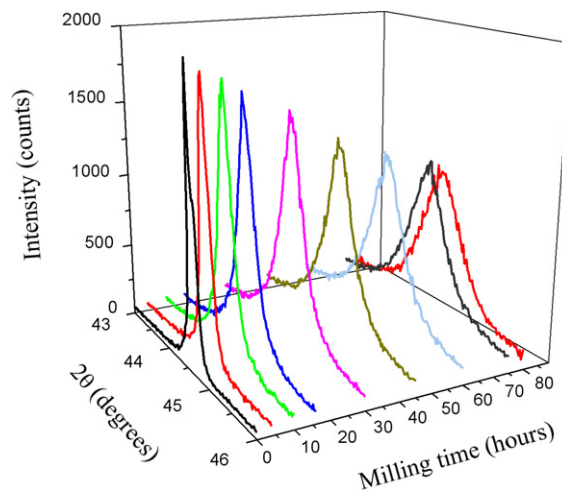

Figure 2. 3D representation of the room temperature XRD intensity versus 2θ ($\lambda = 1.5418$ Å) for the Bragg diffraction reflection (110) as a function of the milling time.

as mentioned in the introduction section. The pattern decomposition for each Bragg peak gives rise to a Williamson–Hall plot [49, 50] that shows an anisotropic broadening, similar to that given by Borbély *et al* based on the momentum method [51]. For this reason, we used a TCH pseudo-Voigt profile with the functions defined by equations (A.5) and (A.6) in the appendix. The XRD patterns collected at RT ($\lambda = 1.5418$ Å) for the Fe-*x*h ($x = 4, 10, 16, 30, 45, 60, 75$ and 80) samples are shown in figure 1. All the diffraction peaks are indexed with a bcc crystal structure (although some impurity traces are observed around $2\theta \sim 35°$, which could be ascribed to Fe oxides, particularly in the patterns corresponding to the samples milled for more than 30 h; see figure 1). The most noticeable features are the decrease of the amplitude and the broadening of the Bragg peaks with the milling time, as can be seen in the 3D representation of the (110) Bragg reflection of figure 2.

The line profile analysis [52] allows us to follow the evolution of the mean size, $\langle \tau_{XRD} \rangle$, and the maximum induced strain, ε, with the milling time at RT, through equations (A.14) and (A.11) (see the appendix). We have to mention that sizes above 200 nm, a distance of the order of the penetration of the x-ray in the samples, are not considered [53], and also that the vertical bars appearing in the mean size and maximum strain (figure 3), and the numbers in parenthesis accompanying the values for these magnitudes (table 1), correspond to a measure of the degree of anisotropy, not to the estimated error. It is evidenced in figure 3 that the τ_{XRD} is reduced rapidly during the first 16 h of milling, down to around 30 nm. Further milling only produces a slow decrease in $\langle \tau_{XRD} \rangle$, to values slightly below 20 nm after 80 h. On the other hand, ε shows a logarithmic-like increase with the milling time, reaching values close to 0.75% for 60 h of milling. This value is almost constant for longer milling times.

For the lattice parameter a similar trend as that of ε is observed (see inset in figure 3 upper part). These findings imply that the milling process produces severe changes in the powder's microstructure. Table 1 summarizes the most relevant
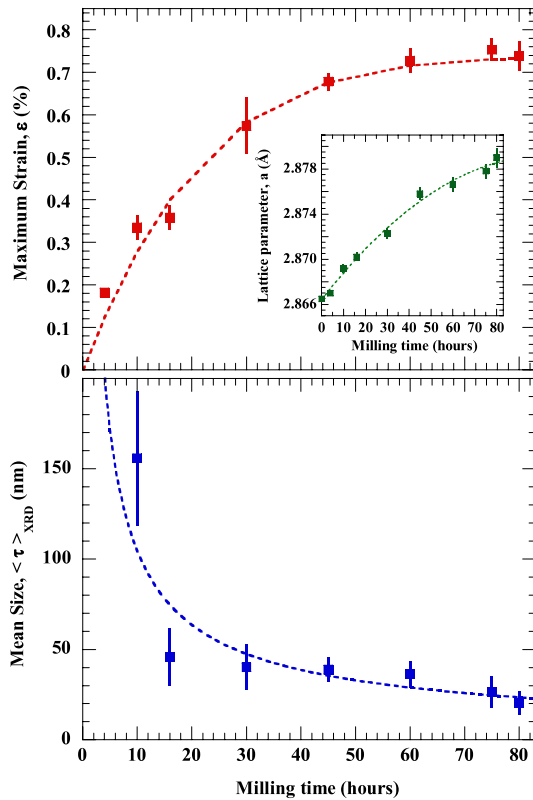
Figure 3. Milling time dependence of the mean size, $\langle\tau_{XRD}\rangle$ (lower panel), and the microstrain, ε (upper panel), for the Fe as-milled powders at room temperature. Vertical bars represent the degree of anisotropy, not the estimated error. The inset in the upper part corresponds to the lattice parameter, a, dependence on the milling time. For more details see the text.

Table 1. Structural data obtained from XRD for the Fe milled samples: lattice parameter, a, mean size, $\langle\tau_{XRD}\rangle$, and maximum strain, ε. The numbers in parenthesis for both $\langle\tau_{XRD}\rangle$ and ε correspond to a measure of the degree of anisotropy, not to the estimated error. The reliability crystallographic R_F-factor and weighted profile R_{wp}-factor are also reported.

Milling time (h)	a (Å)	$\langle\tau_{XRD}\rangle$ (nm)	ε (%)	R_F	R_{wp}
Standard	2.8665 (2)	—	—	5.6	8.3
4	2.8670 (2)	—	—	3.7	5.7
10	2.8692 (3)	160 (93)	0.34 (3)	4.0	5.4
16	2.8702 (3)	45 (15)	0.36 (3)	3.7	4.4
30	2.8723 (4)	40 (12)	0.57 (6)	4.2	5.1
45	2.8758 (5)	39 (5)	0.68 (2)	4.4	5.1
60	2.8766 (6)	36 (7)	0.73 (3)	4.1	4.4
75	2.8778 (6)	25 (8)	0.75 (2)	5.8	6.0
80	2.8790 (8)	20 (5)	0.74 (3)	5.0	6.3

data obtained from the refinement of XRD patterns. In order to confirm these results on the mean size and the maximum strain, additional room temperature XRD patterns using a shorter wavelength ($\lambda = 0.7107$ Å) were collected in both standard and as-milled Fe-80h samples. If we compare figures 1 and 4, the signal-to-background ratio for the Mo radiation is better than that for the Cu one. Apart from this, the number of Bragg reflections in the 2θ-range investigated increases notoriously from six to 29.
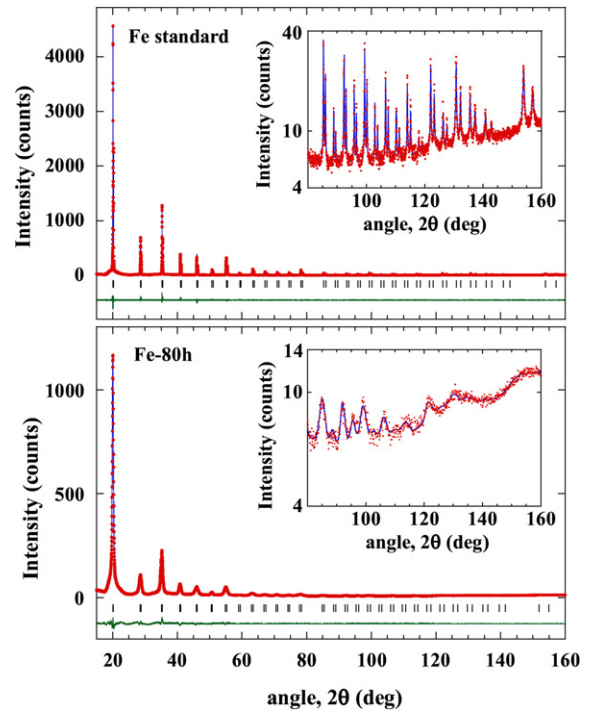

Figure 4. Observed (points) and calculated (solid line) room temperature x-ray powder diffraction patterns of Fe and Fe-80h ($\lambda = 0.7107$ Å). Positions of the Bragg reflections are represented by vertical bars. The observed–calculated difference pattern is depicted at the bottom of each figure. The inset shows the detail in the 2θ-range from 80° up to 160° in a log-scale.

The results found from this short-wavelength XRD are $\langle\tau_{XRD}\rangle = 15 \pm 2$ nm and $\varepsilon = 0.7(1)\%$, in rather good agreement with those obtained from the Cu radiation (see table 1). In figure 5 the histogram showing the grain size distribution of the Fe-80h powders is presented, together with a typical TEM image (see the inset). As mentioned above, the histogram follows quite well a log-normal distribution [54, 55], with values for the mean grain size and the standard deviation of $\langle\tau_{TEM}\rangle = 18 \pm 4$ nm and $\sigma = 10 \pm 2$ nm respectively. Therefore, the values for the average grain size obtained from both XRD and TEM coincide fairly well.

3.2. Microstructural relaxation. The effect of the temperature and the heating rate

In order to study the effect of sample heating on the kinetics of the microstructural thermal relaxation, '*in situ*' NTD experiments at two different heating rates (1 and 10 K min^{-1}) were performed on the Fe-80h as-milled sample. In this case, the used profile function was the TCH pseudo-Voigt one and the IRF was obtained from the analysis of the diffraction pattern at RT corresponding to the Fe standard powder sample. Due to the lower resolution of the D1B diffractometer, an isotropic model for describing the size–strain broadening has been used. Also, we assume now that there is no contribution of the Lorentzian shape to the strain character, thus, in this situation, the working parameters according to the procedure explained in the appendix (see equations (A.1) and (A.2)) are
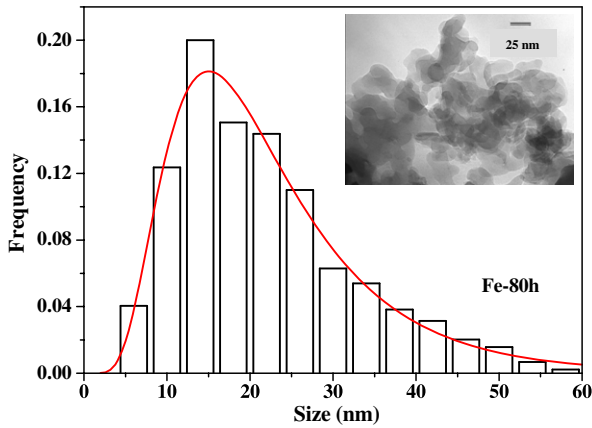
Figure 5. Histogram and log-normal fit (solid line) of the grain size distribution in nanocrystalline Fe-80h determined from TEM micrographs. (One such TEM micrograph is presented in the inset.) The fit parameters are $\langle \tau_{TEM} \rangle = 18 \pm 4$ nm and $\sigma = 10 \pm 2$ nm.

U and Y [56]. The obtained nanoparticle mean size value for the as-milled Fe-80h sample, $\langle \tau_{NTD} \rangle = 19 \pm 2$ nm, is quite similar to those obtained from XRD and TEM, while the maximum strain value, $\varepsilon = 0.78(2)$, is also in good agreement with that obtained from XRD (see table 1). The magnetic moment per Fe atom, calculated from the neutron diffraction pattern at RT, $\mu_{RT} = 1.86(6)$ μ_B, shows a lower value compared with that of the Fe standard sample (2.17 μ_B).

In spite of using an isotropic model for the analysis of microstructure, the NTD patterns are quite well fitted by RM. In figure 6 NTD patterns at four characteristic temperatures together with the fits are depicted. A log-scale for the intensity has been used with the aim of better appreciating the existence of some diffuse scattering around the three first bcc Bragg diffraction reflections, (110) (200) and (211), and additional Bragg contributions associated with some Fe oxide impurities. In these NTD patterns we observe how the broadening (the amplitude) of the Bragg peaks decreases (increases) as the temperature goes up, due to the relaxation of the microstructure in the Fe phase. Also, the existence of a small amount ($\sim 4\%$) of magnetite, Fe_3O_4, or maghemite, γ-Fe_2O_3, has been detected for temperatures above 700 K (see figure 6(b)) [57]. The appearance of this iron oxide takes place during the milling process; however, it is very difficult to observe in the diffraction patterns of the as-milled sample due to the peak broadening of the predominant bcc-Fe phase and the large background signal (see figures 1, 2 and 4). At temperatures above 850 K, Fe_3O_4 transforms into wuestite, FeO (see figure 6(c)). On cooling from 1220 K, the inverse transformation takes place; however, a certain amount of wuestite remains in the sample at RT (see figure 6(d)).

Through the profile broadening analysis we have determined the evolution with temperature of $\langle \tau_{NTD} \rangle$ and ε for both heating rates (see figure 7). The relaxation of the microstructure starts at around 400 K for the slower (1 K min^{-1}) heating rate, while this process starts above 450 K for the quicker (10 K min^{-1}) heating rate. This difference can be explained on the basis of changes in the kinetics of the relaxation process. We observe that the microstrain, ε,
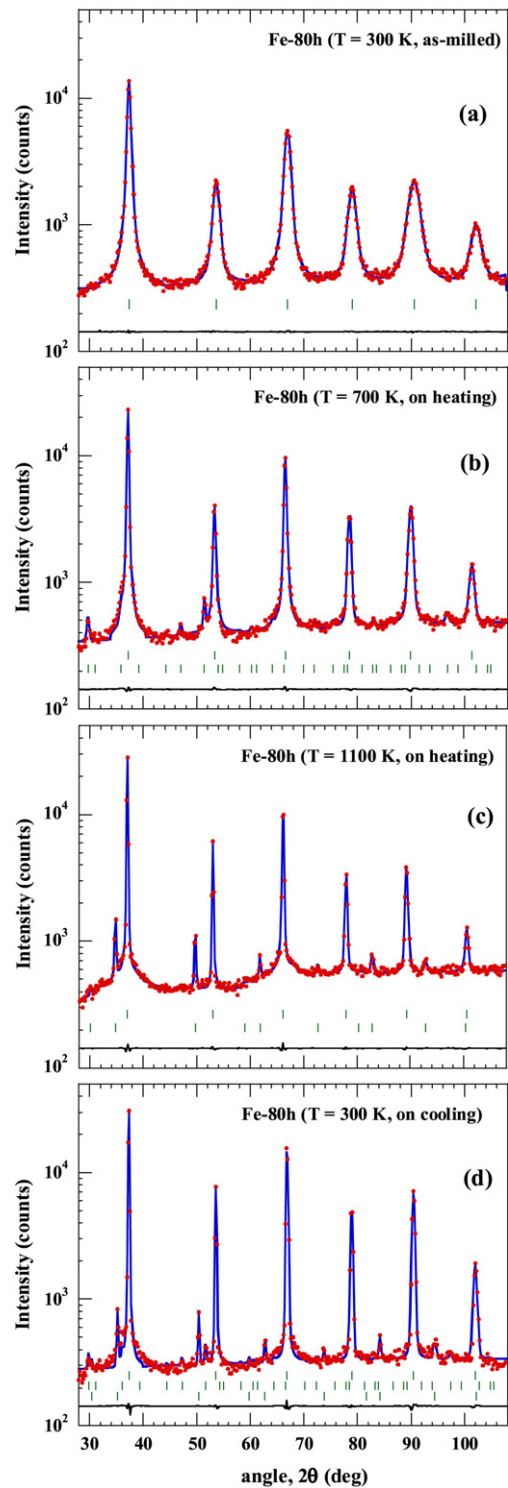
Figure 6. Observed (points) and calculated (solid line) neutron powder diffraction patterns of Fe-80h at different temperatures collected on heating and cooling from RT up to 1220 K and down to RT (see text). Positions of the Bragg reflections are represented by vertical bars (in (a) and (b) the first series of vertical marks corresponds to the nuclear and magnetic contributions; in (c) the second series of vertical marks is associated with Fe_3O_4; while in (d) the third one is related to FeO). The observed–calculated difference pattern is depicted at the bottom of each figure.
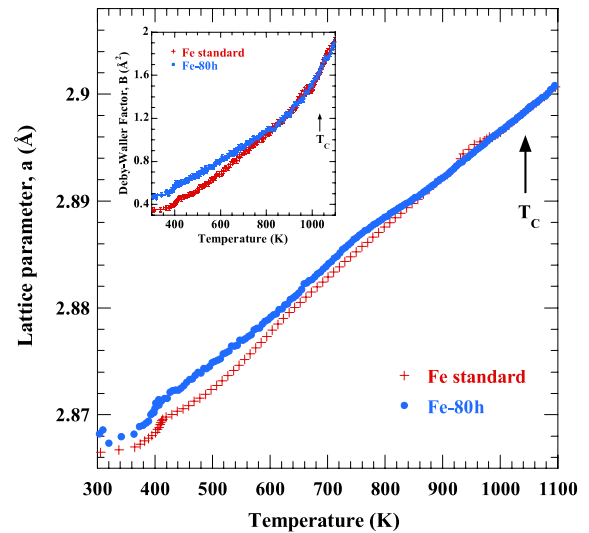
decreases to almost zero values near 850 K (950 K) for the slow (quick) heating rate.
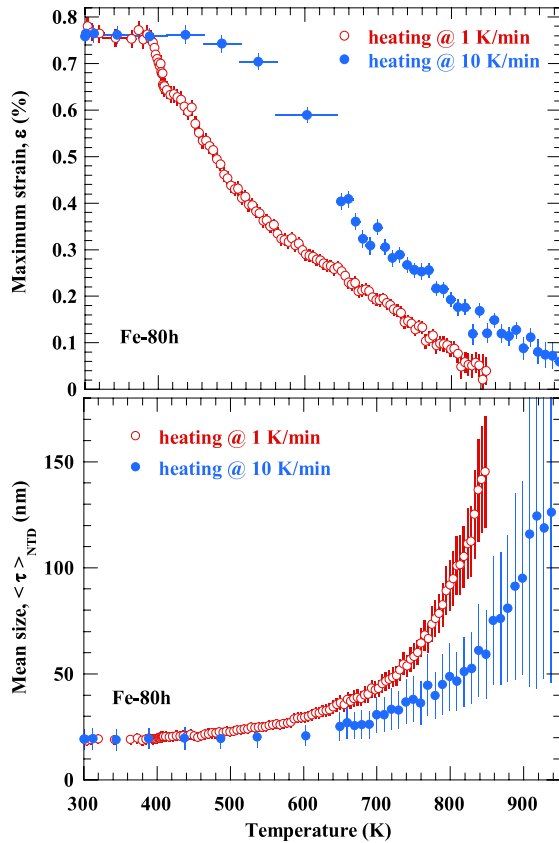
Figure 7. Temperature dependence of the microstrain, ε, and the mean size, τ_{NTD}, for the as-milled Fe-80h sample at 1 and 10 K min^{-1} heating rates.

Figure 8. Temperature dependence of the lattice parameter, a, for Fe standard and as-milled Fe-80h samples at 1 K min^{-1} heating rate The inset shows the temperature dependence of the Debye–Waller factor, B, for both samples.

On the other hand, the value of $\langle\tau_{NTD}\rangle$ remains almost constant below 400 K (450 K) for the slow (quick) heating rates. Further heating above such temperatures gives rise to an increase which follows an exponential-like trend. This grain growth rate is slower for the quicker heating ramp, showing again the influence of the kinetics in the crystalline domain growth due to thermally induced atomic diffusion. There is not enough resolution to consider values of $\langle\tau_{NTD}\rangle$ at temperatures above 900 K (1000 K) for the 1 K min^{-1} (10 K min^{-1}) rate.

The evolution of the macrostrain has been obtained from the comparison between the temperature variation of the lattice parameter, $a(T)$, of the Fe standard powder sample and that corresponding to the Fe-80h (see figure 8). For reasons of clarity we only show the data corresponding to the slow heating rate, 1 K min^{-1}, labelled Fe-80h, and the data of the Fe standard sample. The macrostrain disappears for temperatures above 850 K, the temperature at which the value of the lattice parameter for both samples is nearly the same. The observed trend of both $a(T)$ curves, between 300 and 400 K, where the linear tendency is broken, is due to the thermal inertia of the furnace heater. Moreover, it is worth mentioning that the NTD experiments were carried out up to 1220 K with the aim of observing the reversible bcc–fcc (α–γ) transition, which takes place at 1183 K for pure Fe. It is found that in the case of the Fe-80h powders this transition is also reversible and occurs at the same temperature, suggesting that once the microstructure

of the as-milled Fe has been relaxed, i.e. the powders have lost their nanostructured character, the structural evolution with temperature is analogous to that of pure coarse grained Fe.

Finally, in the case of Bragg–Brentano geometry (XRD patterns) microabsorption parameters must be refined to avoid undesirable errors, especially on the Debye–Waller factor, B, due to the differences in surface roughness and bulk porosity between initial and milled samples [58]. Surface roughness produces a decrease in the intensity of peaks at low diffraction angles that mostly hinder simultaneous refinement with temperature parameters [59]. However, neutron diffraction patterns measured in Debye–Scherrer geometry do not show such microabsorption effects. In this way, the value of B has been estimated from NTD data (0.35 Å^2 for the Fe standard and 0.55 Å^2 for Fe-80h). In the inset of figure 8 is shown the evolution of B as a function of the temperature during the heating for both standard and Fe-80h samples. This heating of the samples gives rise to a continuous increase of B; however, both $B(T)$ curves merge at around 850 K, thus reflecting the end of the microstructural thermal relaxation. The change of the slope at around 1000 K is nothing other than a clear signature of the magnetic transition (ferromagnetic $\rightarrow$ paramagnetic state) of pure bcc-iron.

3.3. Magnetic measurements

The magnetic properties of ball milled Fe have been previously reported by many authors [7–9, 30–32]; however, we have carried out a magnetic characterization of the Fe-80h and the Fe standard samples via $M(T)$ and $M(H)$ measurements in order to correlate structural changes during the heating process with possible magnetic anomalies. In figure 9 the $M(H)$ curve measured at 300 K for the Fe-80h sample is shown. Also, the $M(H)$ curve for the Fe standard powder is presented for comparison. Two main features can be observed in this figure:
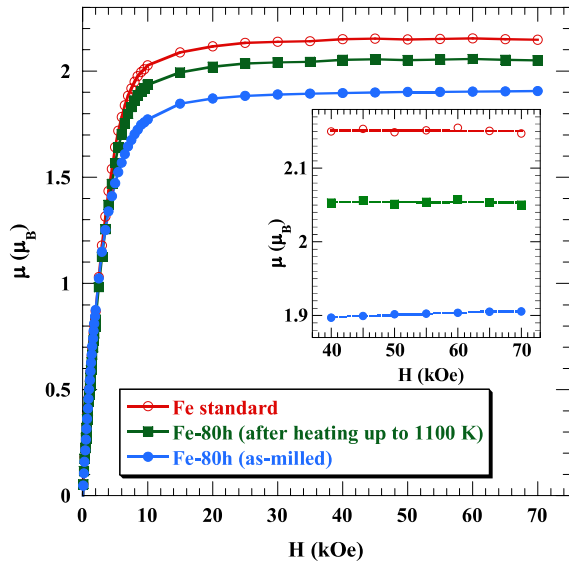
Figure 9. Applied magnetic field dependence of the magnetic moment, μ, measured at room temperature, for the Fe standard powders, the as-milled Fe-80h sample and the latter one after the 290 K–1220 K–290 K heating–cooling process (see text). The inset shows the detail of the dependence of the magnetic moment under high applied magnetic fields.

Figure 10. Temperature dependence of the reduced magnetization (M/M_{RT}) for the Fe standard powders and the as-milled Fe-80h sample (the measurements have been performed on both controlled heating and cooling). M_{RT} is the value of the magnetization measured at RT after heating to 1220 K for both samples. The inset shows the reduced temperature dependence (T/T_C) of the reduced magnetic moment (μ/μ_{RT}, μ_{RT} being the magnetic moment measured at RT) for pure Fe (obtained from [63]) and that of as-milled Fe-80h samples at 1 and 10 K min^{-1} heating rates (obtained from NTD experiments).

first, the $M(H)$ curve for the Fe-80h sample shows lower magnetization values than that of pure Fe, and second, the maximum applied magnetic field, 70 kOe, is easily enough to saturate the standard Fe powders; however, this is not the case for the Fe-80h sample. In this way, we assume that the milling process produces a reduction of the mean value of the magnetic moment for Fe, μ, from 2.17 μ_B (pure Fe) down to 1.9 μ_B. The presence of around 4% of Fe oxides cannot explain this decrease in the magnetic moment of the Fe nanocrystalline phase. Hence, this lower value for the magnetic moment can be attributed to the reduction in the value of μ for the Fe atoms at the grain boundaries mainly due to disorder effects [7, 31, 33, 60]. We must take into account that for a mean crystalline grain size of the order of 20 nm the ratio between the Fe atoms in the 'surface' and in the 'bulk', considering two to three atom layers for the surface, is at least 10–15%; hence, the Fe atoms at the boundaries can play an important role in the total magnetic moment of the sample. On the other hand, we have mentioned the difficulty in saturating the $M(H)$ curve corresponding to the Fe-80h sample (see the inset of figure 9); if we calculate the high field susceptibility, χ_{HF}, of both $M(H)$ curves, we obtain a much larger value in the case of the milled sample, reaching 3×10^{-3} μ_B kOe^{-1}. High values for χ_{HF} are observed in spin-glass-like materials, such as nanostructured Fe, and this feature has been explained on the basis of the existence of ferromagnetic small particles (Fe nanograins) in the presence of magnetically disordered atoms (Fe atoms at the grain boundaries), which makes difficult the saturation of the magnetization even at high magnetic fields [7].

In figure 10 reduced magnetization versus temperature curves, $M/M_{RT}(T)$, for the milled sample measured between 290 and 1100 K on both heating and cooling are presented,

where M_{RT} is the value of magnetization at 290 K after cooling the sample from high temperature. The $M/M_{RT}(T)$ curve of pure Fe powders is also included for comparison, in this case M_{RT} is the value of magnetization of pure Fe at 290 K. This representation in terms of reduced magnetization has been selected in order to better illustrate the differences and similarities of the curvature of the magnetization versus temperature evolution when compared with that of pure Fe. As can be observed in this figure the magnetization value for the as-milled sample is lower than that of pure Fe, in good agreement with $M(H)$ curves of figure 9. However, as the temperature increases, a change in the curve is clearly seen above 600 K, where the $M/M_{RT}(T)$ curve for the as-milled Fe-80h sample tends to overlap that of pure Fe, which occurs above 850 K. This fact can be explained taking into account NTD results; that is, the temperature at which the grain growth begins is around 600 K (see figure 6), giving rise to a decrease of the number of Fe atoms located at the grain boundaries. The microstructural relaxation is nearly finished above 850 K, hence a nanostructured character can no longer be considered. On cooling from high temperature (1100 K) thermo-magnetization curves for both milled and pure Fe samples are indistinguishable, as expected.

Finally, as is well known from a neutron powder diffraction experiment, the magnetic moment direction cannot be deduced for cubic ferromagnets, such as Fe, because any magnetic moment direction with respect to the crystallographic axis gives the same magnetic intensities if the domains are oriented randomly [61, 62]. For this reason, only the magnitude of the magnetic moment can be deduced in this case. The Fe atomic magnetic moment, μ, for the Fe-80h sample has been estimated through the study of the magnetic structure factor in the NTD patterns. In the inset of figure 10

the temperature dependence of the normalized value of μ to its value at RT, $\mu/\mu_{RT}(T)$, for both rates of heating, 1 and 10 K min^{-1}, is presented and compared with that reported for Fe bulk from magnetization measurements [63]. It is worth noting that the magnetic phase transition of the milled samples occur at the expected temperature; that is to say, it is not influenced by the kinetics.

4. Summary

We report on the evolution of the particle size and the induced microstrain with milling time in ball milled Fe powders. These results have been obtained from Rietveld refinement of the room temperature XRD patterns through the analysis of the line broadening. The most noticeable results are (i) a reduction of the mean nanocrystalline size to around 20 nm, in good agreement with the value estimated from TEM images, and (ii) a considerable amount of microstrain (up to 0.7–0.8%) is induced after 80 h of milling time. Furthermore, '*in situ*' neutron powder thermo-diffraction experiments between 290 and 1220 K have revealed that the thermal relaxation of the microstructure begins above 400 K, giving rise to the crystalline grain growth and the diminution of internal microstrain by atomic diffusion, and ends around 850 K. Moreover, we show that this thermal relaxation depends on the heating rate; that is, the kinetics of the structural transformations are clearly different when the heating rate is modified. Above 850 K the milled and bulk Fe merged their physical behaviour, as was found from the temperature dependence of the Debye–Waller factor, the cell parameter and the magnetization.

Acknowledgments

Appendix. Mathematical procedure for the size–strain line broadening analysis

The analysis of the diffraction patterns has been carried out using the FullProf package as mentioned above [42]. The microstructural effects are treated with the integral breadth method using the so-called Voigt model, for both the instrumental and the intrinsic diffraction peak shape. The Thompson–Cox–Hasting (TCH) pseudo-Voigt profile function [64] is used to simulate the exact Voigt function.

The FWHM of the Gaussian, H_G, and Lorentzian, H_L, components of a diffraction peak profile function have an angular dependence given by [41, 54]

$$H_G^2 = \left(U + (1-\xi)^2 D_{ST}^2(\alpha_D)\right)\tan^2\theta + V\tan\theta + W + \frac{I_G}{\cos^2\theta} \tag{A.1}$$

$$H_L = \left(X + \xi D_{ST}(\alpha_D)\right)\tan\theta + \frac{(Y + F(\alpha_Z))}{\cos\theta}. \tag{A.2}$$

Here, U, V, W, X, Y and I_G are refinable parameters and the functions $D_{ST}(\alpha_D)$ and $F(\alpha_Z)$ have different expressions depending on the particular model used for the anisotropic contribution to broadening coming from the strain and the size effects [42, 50]. If we have a standard reference material, V and W must be fixed to zero, then, the rest of the physical meanings of the parameters in the above formula are in terms of strains (U, α_D, X) or size (Y, I_G, α_Z). The parameter ξ is a mixing coefficient measuring the Lorentzian contribution to strains.

The anisotropic strain broadening is modelled using a quadratic form in reciprocal space. This corresponds to an interpretation of the strains as due to static fluctuations and correlations between metric parameters [65]:

$$M_{hkl} = \frac{1}{d_{hkl}^2} = Ah^2 + Bk^2 + Cl^2 + Dkl + Ehl + Fhk. \tag{A.3}$$

The metric parameters $\{\alpha_i\} = \{A, B, C, D, E, F\}$ are considered as stochastic variables with a Gaussian distribution characterized by the mean $\langle\alpha_i\rangle$ and the covariance matrix $C_{ij} = \langle(\alpha_i - \langle\alpha_i\rangle)(\alpha_j - \langle\alpha_j\rangle)\rangle$. The position of the peaks is obtained from the average value of M_{hkl} and the broadening of the reflections is governed by its variance $\sigma^2(M_{hkl})$. In the Stephens' formulation, the 21 correlation terms are grouped, leading to a simplified expression for the variance [66]:

$$\sigma^2(M_{hkl}) = \sum_{i,j} C_{ij} \frac{\partial M}{\partial\alpha_i} \frac{\partial M}{\partial\alpha_j} = \sum_{H+K+L=4} S_{HKL} h^H k^K l^L \sigma^2. \tag{A.4}$$

In our case, the bcc-Fe crystal structure has the Laue class $m\bar{3}m$ and only the parameters S_{400} and S_{220} are different from zero. Finally, the function $D_{ST}(\alpha_D)$, α_D being the set of parameters S_{HKL}, is given by

$$D_{ST}^2(\alpha_D) = 10^{-8} 8\ln 2 \left(\frac{180}{\pi}\right)^2 \frac{\sigma^2(M_{hkl})}{M_{hkl}^2}. \tag{A.5}$$

Concerning anisotropic size broadening it is possible to use a very general phenomenological model, using the Scherrer formula [67], which considers that the size broadening can be written as a linear combination of spherical harmonics (SPH). The anisotropic size is assumed to only contribute to the Lorentzian component of the Voigt function. The explicit formula for the SPH treatment of size broadening is the following:

$$\beta_{\vec{h}} = \frac{F(\alpha_Z)}{\cos\theta} = \frac{\lambda}{\cos\theta} \sum_{mnp} a_{mnp} y_{mnp}\left(\theta_{\vec{h}}, \phi_{\vec{h}}\right) \tag{A.6}$$

being $y_{mnp}(\theta_{\vec{h}}, \phi_{\vec{h}})$ the real SPH with normalization as in [68] and its arguments are the polar angles of the vector $\vec{h} \equiv (h, k, l)$ with respect to the Cartesian crystallographic frame. Through the coefficients a_{mnp} the apparent size along each reciprocal lattice vectors could be calculated.

In the study of the NTD patterns, we used an isotropic model for both strain and size broadening, so only the U, X, I_G

and Y parameters must be taken into account in equations (A.1) and (A.2). Moreover, if we assume that the strain character is described by Gaussian shape and the size broadening by a Lorentzian profile, the parameters X and I_G are zero. From (H_G, H_L), obtained from (1) and (2), we can obtain (H, η) for the pseudo-Voigt function, where the integral breadth is given by

$$\beta_{pV} = \frac{\pi H/2}{\eta + (1 - \eta)\sqrt{\pi \ln 2}} \tag{A.7}$$

and the apparent size $\langle D \rangle_V$ and the so-called maximum strain ε, defined as $1/4$ of the apparent strain η defined by Stokes and Wilson [69], by

$$\langle D \rangle_V = \frac{360\lambda}{Y\pi^2} \tag{A.8}$$

$$\varepsilon = \frac{1}{4} \frac{\sqrt{U\pi}}{2\sqrt{\ln 2}} \frac{\pi}{180}. \tag{A.9}$$

For XRD patterns we used the anisotropic particular functions $D_{ST}(\alpha_D)$ and $F(\alpha_Z)$ shown before. Following a parallel reasoning to the isotropic case, but here permitting a Lorentzian contribution for the strain broadening, we arrive at the next expressions:

$$\langle D \rangle_V^{\vec{h}} = \left(\sum_{mnp} a_{mnp} y_{mnp} \left(\theta_{\vec{h}}, \phi_{\vec{h}} \right) \right) \tag{A.10}$$

$$\varepsilon = \frac{1}{4} \frac{\pi H'_S/2}{\eta_S + (1 - \eta_S)\sqrt{\pi \ln 2}} \frac{\pi}{180}, \tag{A.11}$$

where

$$H'^5_S = [(1 - \xi)^5 + 2.692\,69(1 - \xi)^4\xi + 2.428\,43(1 - \xi)^3\xi^2 \\ + 4.471\,63(1 - \xi)^2\xi^3 + 0.078\,42\,(1 - \xi)\,\xi^4 + \xi^5]D^5_{ST} \tag{A.12}$$

$$\eta_S = 1.366\,03\frac{H_L}{H'_S} - 0.477\,19\left(\frac{H_L}{H'_S}\right)^2 + 0.111\,16\left(\frac{H_L}{H'_S}\right)^3 \tag{A.13}$$

and $\langle D \rangle_V$ can be related to the mean size of the crystallites, $\langle \tau \rangle$, by the expression [70]

$$\langle \tau \rangle = \tfrac{4}{3} \langle D \rangle_V. \tag{A.14}$$

With the aim of obtaining accurate and reliable results from the analysis the best profile and the angular dependence of a standard reference is needed for both x-ray and neutron diffractometers. We have calculated the profile parameters for different standard samples: Si, KCl, Fe, Cu and Ni in the case of the Seifert XRD 3000 diffractometer, and Fe, TiO_2 and Al_2O_3 on the D1B neutron diffractometer.

References

[1] Gleiter H 1989 *Prog. Mater. Sci.* **33** 233
[2] Gleiter H 2000 *Acta Mater.* **48** 1
[3] McHenry M E, Willard M A and Laughlin D E 1999 *Prog. Mater. Sci.* **44** 291
[4] Gorria P, Orue I, Plazaola F, Fernández-Gubieda M L and Barandiarán J M 1993 *IEEE Trans. Magn.* **29** 2682
[5] Gorria P, Garitaonandia J S and Barandiarán J M 1996 *J. Phys.: Condens. Matter* **8** 5925
[6] Gorria P, Prida V M, Tejedor M, Hernando B and Sánchez M L 2001 *Physica* B **299** 215
[7] Bonetti E, Del Bianco L, Fiorani D, Rinaldi D, Caciuffo R and Hernando A 1999 *Phys. Rev. Lett.* **83** 2829
[8] Löffler J F, Braun H B and Wagner W 2000 *Phys. Rev. Lett.* **85** 1990
[9] Del Bianco L, Fiorani D, Testa A M, Bonetti E, Savini L and Signoretti S 2002 *Phys. Rev.* B **66** 174418
[10] Löffler J F, Braun H B, Wagner W, Kostorz G and Wiedenmann A 2005 *Phys. Rev.* B **71** 134410
[11] Randrianantoandro N, Cooper R J, Greneche J-M and Cowlam N 2002 *J. Phys.: Condens. Matter* **14** 9713
[12] Gorria P, Martínez-Blanco D, Blanco J A, Hernando A, Garitaonandia J S, Fernández Barquín L, Campo J and Smith R I 2004 *Phys. Rev.* B **69** 214421
[13] Gorria P, Martínez-Blanco D, Pérez M J, Blanco J A and Smith R I 2005 *J. Magn. Magn. Mater.* **294** 159
[14] Gorria P, Martínez-Blanco D, Blanco J A, Pérez M J, Hernando A, Fernández Barquín L and Smith R I 2005 *Phys. Rev.* B **72** 014401
[15] Benjamin J S and Volin T E 1974 *Met. Trans.* **5** 1929
[16] Ma E and Atzmon M 1995 *Mater. Chem. Phys.* **39** 249
[17] Suryanarayana C 2001 *Prog. Mater. Sci.* **46** 1
[18] Gleiter H, Weissmüller J, Wollersheim O and Würschum R 2001 *Acta Mater.* **49** 737
[19] Zhang D L 2004 *Prog. Mater. Sci.* **49** 537
[20] Koch C C 1997 *Nanostruct. Mater.* **9** 13
[21] Bonetti E, Del Bianco L, Pasquini L and Sampaolesi E 1998 *Nanostruct. Mater.* **10** 741
[22] Chen B, Penwell D, Kruger M B, Yue A F and Fultz B 2001 *J. Appl. Phys.* **89** 4794
[23] Wei Q, Jia D, Ramesh K T and Ma E 2002 *Appl. Phys. Lett.* **81** 1240
[24] Jang D and Atzmon M 2006 *J. Appl. Phys.* **99** 083504
[25] Di Cicco A, Berrettoni M, Stizza S, Bonetti E and Cocco G 1994 *Phys. Rev.* B **50** 12386
[26] Bakker H, Zhou G F and Yang H 1995 *Prog. Mater. Sci.* **39** 159
[27] Rawers J and Cook D 1999 *Nanostruct. Mater.* **11** 331
[28] Costa B F O, Dubiel S M and Cieślak J 2006 *J. Phys.: Condens. Matter* **18** 3263
[29] Meyers M A, Mishra A and Benson D J 2006 *Prog. Mater. Sci.* **51** 427
[30] Ślawska-Waniewska A, Grafoute M and Greneche J-M 2006 *J. Phys.: Condens. Matter* **18** 2235
[31] Del Bianco L, Hernando A, Bonetti E and Navarro E 1997 *Phys. Rev.* B **56** 8894
[32] Fultz B, Robertson J L, Stephens T A, Nagel L J and Spooner S 1996 *J. Appl. Phys.* **79** 8318
[33] Balogh J, Bujdosó L, Kaptás D, Kemény T, Vincze I, Szabó S and Beke D L 2000 *Phys. Rev.* B **61** 4109
[34] Bonetti E, Del Bianco L, Pasquini L, Matteucci G, Beeli C and Signoretti S 2001 *J. Appl. Phys.* **90** 4152
[35] Azzaza S, Alleg S, Moumeni H, Nemamcha A R, Rehspringer J-L and Greneche J-M 2006 *J. Phys.: Condens. Matter* **18** 7257
[36] Rietveld H M 1969 *J. Appl. Crystallogr.* **22** 65
[37] Lutterotti L and Scardi P 1990 *J. Appl. Crystallogr.* **23** 246
[38] Popa N C 1992 *J. Appl. Crystallogr.* **25** 611
[39] Ferrari M and Lutterotti L 1994 *J. Appl. Phys.* **76** 7246
[40] Popa N C 1998 *J. Appl. Crystallogr.* **31** 176
[41] Young R A 1993 *The Rietveld Method* (Oxford: Oxford University Press)
[42] Rodriguez-Carvajal J 1993 *Physica* B **192** 55
[43] Malow T R and Koch C C 1997 *Acta Mater.* **45** 2177
[44] Rawers J, Cook D and Kim T 1998 *Mater. Sci. Eng.* A **248** 212
[45] Yelsukov E P, Lomayeva S F, Konygin G N, Dorofeev G A, Povstugar V I, Mikhailova S S, Zagainov A V and Kadikova A H 1999 *Nanostruct. Mater.* **12** 483
[46] Rixecker G 2002 *Solid State Commun.* **122** 299

[47] Fernández Barquín L, Gómez Sal J C, Gorria P,
     Garitaonandia J S and Barandiarán J M 1998 *J. Phys.:
     Condens. Matter* **10** 5027
[48] Fernández-Martínez A, Gorria P, Cuello G J, Santos J D and
     Pérez M J 2007 *J. Non-Cryst. Solids* **353** 855
[49] Williamson G K and Hall W M 1954 *Acta Metall.* **1** 22
[50] Rodriguez-Carvajal J and Roisnel T 2004 *Mater. Sci. Forum*
     443/444 123
[51] Borbély A, Révész A and Groma I 2006 *Z. Kristallogr.*
     2006 (Suppl. 23) 87–92
[52] Langford J I and Louër D 1996 *Rep. Prog. Phys.* **59** 131
[53] de Keijser Th H, Langford J I, Mittemeijer E J and
     Vogels A B P 1982 *J. Appl. Crystallogr.* **15** 308
[54] Armstrong N, Kalceff W, Cline J P and Bonevich J 2004
     Diffraction Analysis of the Microstructure of Materials
     ed E J Mittemeijer and P Scardi (Berlin: Springer)
[55] Snyder R L, Fiala J and Bunge H J 1999 *Defect and
     Microstructure Analysis by Diffraction* (Oxford: Oxford
     University Press) and references therein
[56] Wilson A J C 1962 *X-ray Optics* 2nd edn (London: Methuen)
[57] Löffler J F, Meier J P, Doudin B, Ansermet J-P and
     Wagner W 1998 *Phys. Rev.* B **57** 2915
[58] Pitwsche W, Hermann H and Mattern N 1993 *Powder Diffact.* **8**
     74
[59] Pitwsche W, Mattern N and Hermann H 1993 *Powder Diffact.* **8**
     223
[60] Wagner W, Wiedenmann A, Petry W, Geibel A and
     Gleiter H 1991 *J. Mater. Res.* **6** 2305
[61] Shirane G 1959 *Acta Crystallogr.* **12** 282
[62] Blanco J A, Espeso J I, García Soldevilla J, Gómez Sal J C,
     Ibarra M R, Marquina C and Fischer H E 1999 *Phys. Rev.* B
     59 512
[63] Cullity B D 1972 *Introduction to Magnetic Materials*
     (Reading, MA: Addison-Wesley) p 617
[64] Thompson P, Cox D E and Hastings J B 1987 *J. Appl.
     Crystallogr.* **20** 79
[65] Rodríguez-Carvajal J, Fernández-Díaz M T and Martínez J L
     1991 *J. Phys.: Condens. Matter* **3** 3215
[66] Stephens P W 1999 *J. Appl. Crystallogr.* **32** 281
[67] Warren B E 1969 *X-ray Diffraction* (Reading, MA:
     Addison-Wesley)
[68] Jarvinen M 1993 *J. Appl. Crystallogr.* **26** 527
[69] Stokes A R and Wilson A J C 1944 *Proc. Phys. Soc.* **56** 174
[70] Langford J I, Louër D and Scardi P 2000 *J. Appl. Crystallogr.*
     33 964